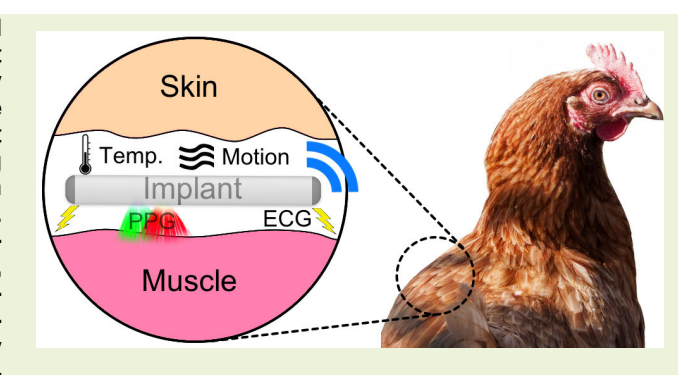


A Subcutaneously Injectable Implant for Multimodal Physiological Monitoring in Animals

Parvez Ahmmed¹⁰, *Member, IEEE*, James Reynolds¹⁰, *Member, IEEE*, and Alper Bozkurt[®], Senior Member, IEEE

Abstract—Unobtrusive acquisition of physiological and behavioral data from freely moving animals is important to many applications including animal research, veterinary science, animal husbandry, and pet monitoring. This article reports a miniaturized, injectable, and multimodal implant for real-time measurements of heart rate (HR), breathing rate (BR), movement, and subcutaneous temperature with future extensions to blood pressure and oxygen saturation. To estimate these vital signs, the presented device incorporates sensors of various modalities: photoplethysmography, electrocardiography, accelerometry, magnetometry, and thermometry. A rechargeable battery drives the system containing a system-on-chip with Bluetooth low energy capability and multiple sensor front-end circuits. The implant electron-



ics are isolated from the animal's extracellular fluid by a dual-layer encapsulation of biomedical epoxy and poly(methyl methacrylate) that fits into a six-gauge surgical needle to allow for subcutaneous injection. Electrically conductive epoxy is used to create electrodes on the surface of the encapsulation for biopotential measurements. With a 3-m wireless range from a custom receiver, this implant can continuously transmit data from all the sensors for 20 h, which can support two-three months of duty-cycled and intermittent recording between battery recharges. The system was tested in vivo where the acquired HR and BR estimations showed an error of less than two beats per minute (BPM) compared to the gold standard. Longer-term evaluation of tissue reaction showed an acceptable level of immune responses with minimal effect on the sensing performance. This novel system has the potential to provide new insights with greater depth in veterinary research and practice, and animal welfare management.

Index Terms—Accelerometers, animal welfare, biocompatibility, biophotonics, cardiovascular health, electrocardiography (ECG), injectable implant, photoplethysmography (PPG), physiological monitoring, polymer encapsulation, temperature measurement.

I. Introduction

♦ ONTINUOUS health monitoring in animals continues to gain momentum and be a game-changer in many application areas from proactive healthcare management to

Manuscript received 17 November 2023; revised 1 February 2024; accepted 9 February 2024. Date of publication 22 February 2024; date of current version 2 April 2024. This work was supported by the National Science Foundation (NSF) under Grant IIS-2319060, Grant IIS-2037328, Grant EF-2319389, Grant CCSS-1554367, and Grant ECC-1160483 NSF Nanosystems Engineering Research Center for Advanced Self-Powered Systems of Integrated Sensors and Technologies (ASSIST). The associate editor coordinating the review of this article and approving it for publication was Dr. Jürgen Kosel. (Parvez Ahmmed and James Reynolds contributed equally to this work.) (Corresponding author: Alper Bozkurt.)

This work involved human subjects or animals in its research. Approval of all ethical and experimental procedures and protocols was granted by the Institutional Animal Care and Use Committee (IACUC) of NC State University.

The authors are with the Department of Electrical and Computer Engineering, North Carolina State University, Raleigh, NC 27695 USA (e-mail: pahmmed@ncsu.edu; james.reynolds@ncsu.edu; aybozkur@ ncsu.edu).

Digital Object Identifier 10.1109/JSEN.2024.3366195

tracking outbreaks of infectious diseases. Acquiring and studying vital signs like heart rate (HR), breathing rate (BR), blood pressure (BP), oxygen saturation (SpO₂), and core-body temperature, and behavioral traits (e.g., activity levels and sleep patterns) from freely moving animals can provide significant insights to veterinarians, animal owners, and researchers [1], [2], [3], [4], [5], [6]. Moreover, these insights have the potential to provide a holistic view of an animal's welfare and ensure correct strategies for healthy living and stress management [7], [8], [9], [10]. The livestock industry, which is currently undergoing a massive transformation driven by consumer concerns for welfare-friendly husbandry systems, can specifically benefit from continuous physio-behavioral monitoring [11], [12], [13], [14].

New wearable devices have been becoming more popular to meet the health-tracking needs of a wide variety of animals ranging from livestock to pets [15], [16], [17]. These systems must consider the challenge of externally attaching bulky devices to freely moving animals, such as the adverse impact on animals' natural behavior and comfort [18], which

1558-1748 © 2024 IEEE. Personal use is permitted, but republication/redistribution requires IEEE permission. See https://www.ieee.org/publications/rights/index.html for more information.

introduces what is known in animal research as the Hawthorne effect. The animals themselves or other animals in a group tend to damage or disassemble the wearable devices. Moreover, the quality of the data recorded from externally attached sensors can suffer due to the obstruction created by the thick layers of skin and fur [19]. Implantable devices, on the other hand, can be minimally intrusive and provide a better coupling with the tissue for higher quality sensor measurements [20].

Several implantable monitoring systems with various sensing modalities are available commercially and have been presented in the literature. Biophotonic sensor systems for measuring arterial blood volume (photoplethysmography (PPG) or pulse oximetry) are best suited for the implantable form factor because of the myriad of derivable vital signs (e.g., HR, BR, and SpO₂) as well as simpler packaging requirements [21], [22], [23]. Another commonly used modality is arterial-pressure sensing which requires the device to be placed on the blood vessels [24], [25]. Biopotential sensors for electrocardiography (ECG) provide a deeper insight into the cardiovascular health of an animal, but making provisions for the electrically conductive electrodes outside an encapsulated implant has been a concern [26], [27], [28]. However, if such a provision can be implemented, a combination of biophotonic and biopotential measurements can enable more reliable estimations of HR and BR and allow the extraction of additional exploratory health parameters like pulse transit time (PTT) which is correlated to BP and stress levels [29]. Recording core-body temperature is common in commercially available data loggers such as the E-mitter (Starr Life Sciences Corporation, Oakmont, PA, USA), DST milli-HRT (Star Oddi, Gardabaer, Iceland), and Thermochron iButtons (Maxim Integrated, San Jose, CA, USA) [30], [31]. Lastly, a considerable number of implants with motion sensors for tracking animal behavior are also documented [32], [33], [34].

Other than the commercial implants, only a few designs presented by academic researchers have demonstrated an in vivo, end-to-end, standalone wireless operation [25], [26], [27], [28], [35]. The majority of these provide a single modality of sensing in relatively bulky form factors that require an elaborate surgical procedure to implant the devices. A miniaturized injectable system implantable through a small incision could benefit from the ease of insertion as well as the intrinsic advantages of a subcutaneous sensor system by avoiding attenuation from fur, skin, and lipid layers [36].

This article presents the most advanced multimodal and minimally invasive injectable sensor system for animals to wirelessly monitor several of their physiological indicators and activity patterns. The presented multimodal implant (Fig. 1) is capable of subcutaneously measuring PPG, ECG, bioimpedance (BioZ), accelerometry (ACC), magnetometry (MAG), and thermometry (TMP). The components for the sensors and the analog front-end (AFE) circuits are suitably chosen from the commercial off-the-shelf (COTS) integrated circuits (ICs) to reduce developmental time and cost compared to an application-specific IC [37], [38]. All the AFEs, along with a wireless system-on-a-chip (SoC) and battery, are packaged into a 52-mm-long capsule-shaped cylinder with

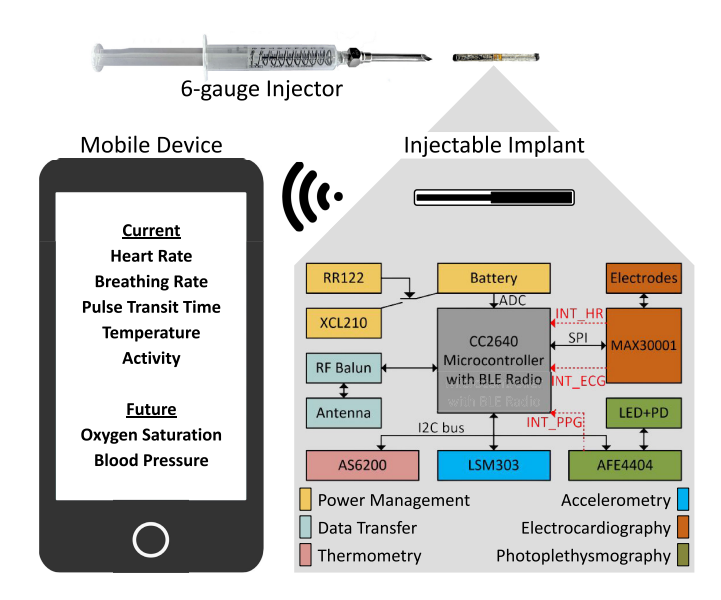


Fig. 1. System block diagram of the presented injectable health monitoring system with a simplified schematic describing the subsystem components.

a diameter of 4 mm. This size of the implant fits into a commercially available standard six-gauge surgical needle and allows for an easier implantation method that minimizes the incision size. The contributions of this article include the addition of biopotential hardware, packaging innovations to accommodate electrode interfaces for bioelectric measurements and to enhance biocompatibility, a significant reduction of power consumption by the implant's electronics, and the development of a receiver platform for data aggregation with respect to the earlier versions of the system [39], [40]. Sections II–IV contain a description of the implant's hardware development, embedded software, and manufacturing techniques, respectively. Several in vivo experiments have ensured the functionality, usability, and reliability of the sensor system as discussed in Section V.

II. SYSTEM OVERVIEW

A. Injectable Sensor System

The developed injectable electronic system includes various sensors, front-end circuits, a microcontroller with a wireless radio system, and a power management unit (Fig. 1). Our earlier design had a printed circuit board (PCB) size of 3.6×30 mm [40]. This new design retained all of those previously discussed components along with the inclusion of a new ECG and BioZ AFE and other circuit strategies such that the system is still the same size as before. All these components are briefly discussed in this section as a comprehensive description of the hardware.

1) SoC With a Microcontroller and Radio: The embedded system is built around an integrated SoC (CC2640, $2.7 \times 2.7 \times 0.5$ mm, Texas Instruments, Dallas, TX, USA) equipped with three microprocessors, a Bluetooth low energy (BLE) wireless transceiver, and other peripherals. The microcontroller activates and configures the AFEs on demand and transfers recorded data wirelessly. The three processors in the microcontroller are: 1) the main ARM Cortex-M3 processor

maintaining the program flow and communicating with the other two processors; 2) an ARM Cortex-M0 processor handling the BLE radio communication; and 3) a custom core [sensor controller (SC)] allowing for reduced energy usage while communicating with the on-board sensors.

The choice of an appropriate antenna is critical for the efficient wireless performance of the system. First, the size constraints of the implant force the selection of a chip antenna despite its lower transmission efficiency compared to a trace antenna laid out on a PCB. Moreover, the proper operation of RF antennas (both chip and trace) depends on the area of metal clearance underneath the antenna [41]. The size of our implant does not allow for a large, empty area around the antenna. The design requires an antenna that would still work with traces running underneath it. We chose an integrated RF antenna (2450AT, $5.0 \times 2.0 \times 1.5$ mm, Johanson Technology, Inc., Camarillo, CA), which is designed for 2.4-GHz communication and is impedance-matched using a balun (2450BM, $1.6 \times 0.8 \times 0.6$ mm, Johanson Technology, Inc.) to reduce the component count.

2) PPG Subsystem: The core components of the PPG subsystem include light-emitting diodes (LEDs), a photodiode (PD), and AFE circuitry. Our miniaturized system uses an integrated package (SFH7050 BioMon Sensor, $4.7 \times 2.5 \times 0.9$ mm, OSRAM Opto Semiconductors GmbH, Regensburg, Germany) with three LEDs (green at 525-nm wavelength, red at 660-nm wavelength, and infrared at 950-nm wavelength) and one PD. The optical sensor is placed at the bottom side of the PCB to capture the photons backscattered from the tissue. The selected AFE (AFE4404, Texas $2.6 \times 1.6 \times 0.5$ mm, Instruments) serves purposes: controlling the pulsing and current level of the LEDs and amplifying and digitizing the photo-current generated by the PD. The AFE time-multiplexes the LEDs through sequential pulsing to deploy multiple wavelengths in rapid succession along with a dark period for measuring the ambient light level and dark noise. Both the configuration registers and the analog-to-digital converter (ADC) data registers are accessible via the interintegrated circuit (I²C) communication protocol.

3) Biopotential and BioZ Subsystem: The biopotential and BioZ AFE circuit (MAX30001, 2.9 × 2.7 × 0.6 mm, Maxim Integrated) can amplify the ECG and BioZ signals coming from a two-electrode or four-electrode configuration. In our design, two electrodes, filtered through a network of passive components, are connected to this AFE. The IC has an internal first-in-first-out (FIFO) memory for raw ECG and BioZ data and provides data-ready interrupts to read the collection of samples together over the serial peripheral interface (SPI) bus. This AFE is also equipped with the built-in capability to detect R-to-R intervals using an adaptation of the Pan–Tompkins peak detection algorithm [42]. This would potentially enable users to turn off the raw biopotential data acquisition and operate in a lower energy mode by only recording the HR.

The electrode design is critical for accurately measuring biopotentials. The challenges involved with creating an adequate electrode connection with the tissue include having a sufficient surface area while bridging external electrodes

with encapsulated electronics inside a waterproof enclosure. Existing biopotential electrode designs in the literature address this with micromachined metal or spiraled wire as the conductive electrode and melted glass or cured epoxy as the waterproof encapsulation [43], [44], [45]. The primary drawback of using metal electrodes for this application is the difficulty and expense of machining the metal to fit the 4 mm diameter. A spiral wire would help to anchor the implant but brings significant concerns related to long-term rigidity when subjected to forces exerted on it under an animal's skin and providing limited tissue contact. Our earlier design utilized a novel additive manufacturing technology, NeuroStone [46] from Murata Manufacturing Company Ltd., Kyoto, Japan, along with glass tube encapsulation which had a diameter of 6 mm [47]. In an attempt to fit the smaller size constraint, we also demonstrated custom-designed electrodes made of conductive epoxy with sufficient performance for recording biopotentials [48].

4) ACC and TMP Sensors: An ultralow-power triaxial accelerometer (LSM303, $2.0 \times 2.0 \times 1.0$ mm, STMicroelectronics, Geneva, Switzerland) is used to detect movements. This eCompass module, additionally, includes a triaxial magnetometer providing orientation information, which can be useful for various behavioral monitoring applications. This IC is also equipped with programmable configuration registers and internal FIFO memory. Although LSM303 has a built-in temperature sensor, a separate Si-bandgap-based sensor (AS6200, $1.5 \times 1.0 \times 0.6$ mm, ams AG, Premstätten, Austria) is used for better measurement resolution. Both the sensors communicate with the microprocessor via the I²C protocol.

5) Power Management Subsystem: The power subsystem features a dc-dc converter and an external switching mechanism. This system uses a step-down buck conversion topology with a single voltage output of 1.8 V (XCL210, $2.5 \times 2.0 \times 1.0$ mm, Torex Semiconductor Ltd., Chuo City, Tokyo, Japan). The choice of this regulator is dominated by its higher conversion efficiency and minimal usage of external components. We included a magnetic sensor (RR122, $1.4 \times 1.4 \times 0.45$ mm, Coto Technology, Inc., North Kingstown, RI, USA) as a switch to control the operation of the power supply remotely from outside the tissue. With a permanent magnet outside the animal's body, the system can be completely shut off (except for the switch itself) when the magnet is brought near to the implant. This feature allows for the implant to be stored for long periods and provides a way to reset the entire system if needed.

The size of the power storage (batteries) is one of the greatest challenges within the constraints of our application. Previously, we had used CR425 and CR435 batteries that have a nominal voltage of 3.0 V [40]. The CR pin-type batteries have a lower self-discharge rate and a more compact construction making them suitable for our application. A few drawbacks with those batteries were the inability to be recharged, limited shelf life, difficulty in soldering the terminals, and the nominal voltage being marginally suitable for the green LEDs. In this design, we used a 15-mAh rechargeable Li-ion pin-type battery (CG-320B, Panasonic Corporation,

Kadoma, Osaka, Japan) with solder-friendly terminals and a nominal voltage of 3.8 V. This cylindrical battery has a length of 20 mm, and its diameter is 3.65 mm. Finally, to remotely monitor the battery voltage (BAT) in real time, the battery terminals are connected to one of the ADC channels of the microcontroller through a resistive divider.

B. Data Aggregation System

The use of BLE for wireless communication not only reduces power consumption but also allows a wide variety of compatible devices to connect for external data aggregation. Various externally controlled BLE connection parameters determine the overall power consumption of the implant system. The proprietary driver libraries in most commercially available devices (e.g., laptops and smartphones) do not allow complete control over these parameters. Hence, we designed a custom BLE receiver system as the external data aggregator.

The external data aggregation system is developed with a wireless microcontroller (CC2642, $7.0 \times 7.0 \times 1.0$ mm, Texas Instruments). Along with the other two processors for BLE radio and SC, similar to CC2640 used in the implant as the SoC, this microcontroller has an ARM Cortex-M4F processor as the core processing unit. The advanced core and larger capacity of the Flash, ROM, and SRAM memories allow for more sophisticated data acquisition software.

As there are no restrictions concerning the size of this external data acquisition system, we used a higher gain (1.3 dBi) antenna (2450AT, $9.5 \times 2.0 \times 1.2$ mm, Johanson Technology, Inc.) from the same series of surface-mount RF antennas that we used in the implant along with the same impedance-matching balun (2450BM, $1.6 \times 0.8 \times 0.6$ mm, Johanson Technology, Inc.). This extra boost improves the wireless range. The data storage consists of a microsized secure digital (micro-SD) memory card included on the board.

The external receiver system is powered by a 480-mAh lithium-ion polymer (LiPo) battery for portable operation or a micro-USB power supply for a wired connection. Charging circuitry (MCP73831, $3.0 \times 2.0 \times 0.9$ mm, Microchip Technology, Inc., Chandler, AZ, USA) recharges the LiPo battery using the same micro-USB power supply. This whole system can be placed anywhere within the wireless range of the implant, can operate untethered or plugged into a wall charger, and can even be placed on the animal through a backpack for free-range monitoring applications.

III. EMBEDDED SOFTWARE

The embedded system software for both the implant (peripheral role) and the data aggregator (central role) is built around the Texas Instruments SimpleLink BLE5 Protocol Stack. The applications are implemented with the TI-RTOS kernel that runs the software solution with task synchronization between the application running on the main processor and the BLE5-stack running on the Cortex-M0 processor. However, our final system has discarded most of the optional BLE features (e.g., device pairing and parameter update) to fit the application software, which controls all the sensors, into the available memory space of CC2640.

A. Sensor Implant (BLE Peripheral)

The application in the implant system initializes the BLE peripheral characteristic profiles, the SC application, I²C and SPI drivers, and the external hardware with all the sensors in sleep mode. Thereafter, the implant broadcasts its identity at a certain advertising interval. After a BLE central device (the external data aggregator) establishes a connection with the implant, it can send configuration commands through a BLE characteristic channel to enable and disable individual AFEs, write to and read from their programmable registers, etc. This enables the central device to control almost every aspect (e.g., gain and sampling rate) related to the sensor configuration.

Most of the sensor configurations are predetermined and loaded during the activation of the sensors. However, a few parameters need to be configured at run time. For example, PPG signals are very sensitive to ambient light and the amount of contact pressure. Hence, the amplifier gain and the bias-canceling current need to be dynamically configured to avoid the saturation of the PPG signal. The central device could potentially perform this task of calibrating these settings, but we chose to implement it in the peripheral device to reduce wireless activity as it is not a computationally expensive task.

Once one or more of the implant's sensors are initialized by the central device, the sensor ICs start to sample at a specific recording rate and store those into the AFEs' internal FIFO memory, if available. The microcontroller reads these sensor data by responding to the hardware interrupts (either dataready or FIFO-full alerts) and writes the recorded data in the corresponding characteristic data buffer. When a data buffer is full (96-B data followed by a 4-B timestamp, in our design), the application sends a notification to the BLE central device. The use of these long characteristic buffers, which is a new feature of the BLE5 Stack, helps reduce BLE transfer overload, thereby reducing the energy requirement.

When not actively interacting with the AFEs or communicating via BLE, the main processor remains in sleep mode consuming minimal power. The processor can wake up from the hardware interrupts generated by the sensor ICs, periodic timers, or radio events, and these active periods use a substantial amount of supply current. In order to minimize the system-level power consumption, the number of interrupting events needs to be minimized. Primarily, we enforced this by utilizing the available FIFO memory in the sensor ICs and reading the data in burst I²C/SPI mode. The FIFO-full interrupts are received when the FIFO is full up to a userdefined "watermark" level. In our specific case, the PPG and MAG AFEs lack any FIFO memory and thus send more frequent data-ready interrupts. This is where the low-power custom core of the SC becomes useful. The SC application reads and accumulates the sensor data by responding to the hardware interrupts and notifies the main processor only when the data buffers are full which contributes toward the reduction of the execution time of the main processor. Thus, the power consumption of the implant system is significantly reduced by transferring some of the sensor interfacing tasks to the SC (Fig. 2).

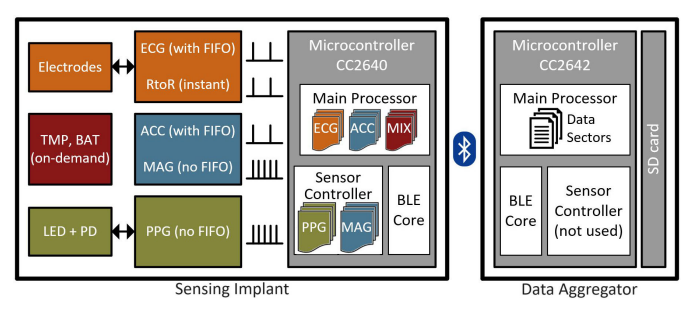


Fig. 2. Block diagram showing the flow of data from all the sensors through the five characteristic buffers to the micro-SD card sectors. As the PPG and MAG sensors have no FIFO, the low-power SC responds to the frequent interrupts and notifies the main CPU when the data buffer is full.

B. Data Aggregator (BLE Central)

The application in the central data aggregator initiates by configuring the on-board micro-SD card and a two-button menu system, accessible through a universal asynchronous receiver/transmitter (UART) terminal, in separate task stacks. The menu system can be used to discover, connect to, and access peripheral devices. Even when the UART host is not connected, the device automatically scans for available BLE peripheral devices around and looks for a specific universally unique identifier (UUID) assigned to the implants for a certain interval repeatedly. Once it finds the advertising implants, it tries to connect to the nearest one based on the highest value of the average received signal strength indicator (RSSI).

After the Bluetooth connection is established, the application discovers all the characteristic profiles defined in the implant and registers to their notifications. The central device then enables the sensors in the implant with the required configurations and starts receiving the data stream through BLE notifications. The program accumulates the data from different characteristics with an appropriate identifiable header (characteristic handle and data length) in a 512-B data buffer. When the buffer is full, it is written to the micro-SD card, one sector at a time.

IV. IMPLANT ENCAPSULATION

The implant packaging has to account for multiple separate design objectives: 1) electrical and mechanical isolation between the electronics and the wet environment of the body's extracellular fluid; 2) optical clarity and transparency for PPG; 3) electrically conductive contact with the tissue for biopotential recording; and 4) radiolucency for wireless communication. The design efforts presented in this article provide improved strategies for each of these factors [40].

The implant is intended to fit within a six-gauge surgical needle. We used poly(methyl methacrylate) (PMMA), also known as acrylic, for constructing the bulk of the implant enclosure. Along with the fundamental advantages in terms of transparency and biocompatibility, this thermoplastic can also be cast in a mold. Before being embedded in PMMA, the surface-mounted components on the PCB are covered by a layer of biomedical epoxy (LOCTITE¹ EA M-31CL, Henkel

Corporation, Düsseldorf, Germany). The battery is also coated with this biomedical epoxy (see Fig. 3).

The PMMA is cast around the core in an open concave mold (see Fig. 4) made of polydimethylsiloxane (PDMS). This mold is created using a solid cylindrical template, printed using additive manufacturing, with the same dimensions as the implant. The PDMS is poured around it. After 24 h of cure time, the template is removed, and the resulting mold is heat-treated.

The implant enclosure assembly starts with a thin layer of biomedical epoxy curing over the circuit board except for over the ECG input pads where insulated tin-plated copper wires are soldered to connect with the electrodes outside. The epoxy-coated battery (CG-320B) is also attached to the board by soldering one end directly and the other end through a piece of enameled magnet wire. If the battery is not solder-friendly (e.g., CR425 and CR435), it is held in place at the end of the board by an ethyl cyanoacrylate gel (LOCTITE¹ superglue, Henkel Corporation) while an electrically conductive adhesive cures to form a connection with the terminals. The device is then put into the concave PDMS mold with the electrode wires coming out of the two ends and the optical components facing the flat side. The mold's open-top structure has several advantages. First, it provides enhanced optical clarity due to the surface tension. Second, the flat edge limits the light distortion into and from the tissue. Finally, it helps keep the device in place by limiting rotation. After the PMMA has cured, the wires coming out of the encapsulation are curled up and covered with a lump of conductive epoxy, either silverbased (H20E, Epoxy Technology, Inc., Billerica, MA, USA) or carbon-based (CCC Carbon Adhesive, Electron Microscopy Sciences, Hatfield, PA), to form the electrodes having approximately the same size as previously demonstrated [48].

All these carefully selected materials allow the implant to be refurbished as they dissolve when immersed in acetone and the process can be adjusted using the acetone exposure duration. Usually, an hour of immersion helps to dissolve the PMMA and cyanoacrylate around but not the inner layer of biomedical epoxy that protects the components from damage during this process. The same electronics can be coated again with PMMA in order to use the system again.

V. EXPERIMENTS AND RESULTS

We performed several in vitro and in vivo experiments to evaluate the implant's system-level performance and validate the recorded sensor data. All the animal procedures were approved by the Institutional Animal Care and Use Committee (IACUC) of NC State University, Raleigh, NC, USA, and handled by experienced veterinarians.

A. Wireless Range

The wireless range of the Bluetooth interface depends on several factors such as transmission power, antenna efficiency, and surrounding environment. To optimize the system for low-power operation, we reduced the transmission power to 0 dBm. As discussed earlier, the on-ground antenna has lower efficiency than the usual ground-clearance antennas.

¹Registered trademark.

Fig. 3. Side view of the implant showing the two-layer packaging on the electronics and the battery with the conductive epoxy electrodes at the ends. The optical components and the temperature sensor are placed on the bottom side to ensure optimal tissue contact, and the antenna is placed on the top side to reduce transmission loss.

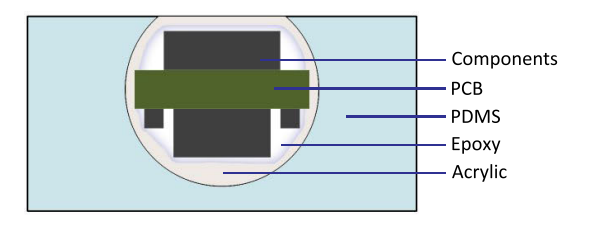


Fig. 4. Cross section of the PDMS mold with the epoxy-coated implant immersed in an acrylic casting in a "D"-shaped cavity.

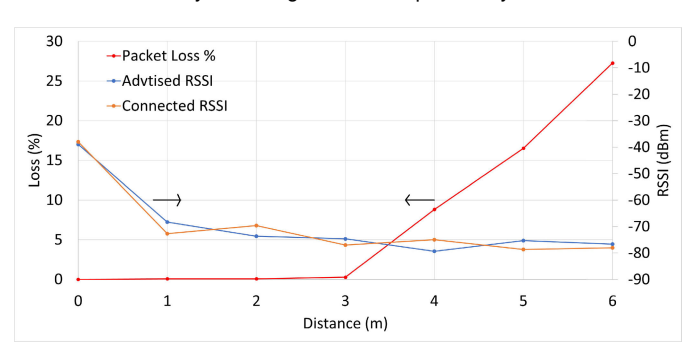


Fig. 5. RSSI level measured by the external central BLE data aggregator device while the implant is advertising or in a connected state. The percentages of missed notifications at different distances are also presented.

Thus, we expected the range of the system to be lower than the industry-standard Bluetooth specifications. We ran experiments to characterize the limits of our system.

First, we recorded the RSSI of an encapsulated implantable device at various distances from the central device away from other interfering devices in an open outdoor field. The bare devices were placed on top of two stages made out of wooden material which were moved to increase the distance in-between. Thanks to the relatively omnidirectional radiation pattern of the used COTS antenna, no specific orientation for the antenna was chosen during the measurements other than ensuring the implant and data aggregator antenna sides face each other. When the BLE central device discovers a peripheral device, it automatically reads the advertising RSSI. After the connection is established, the central device can also read the RSSI levels periodically using the protocol stack. As shown in Fig. 5, both the RSSI levels dropped with increasing distance.

Afterward, we counted the number of notifications sent by the peripheral devices $(N_{\rm sent})$ and the number of data packets received by the central device $(N_{\rm received})$ for a certain duration. From there, we calculated the packet loss by using

Packet Loss =
$$\frac{N_{\text{sent}} - N_{\text{received}}}{N_{\text{sent}}} \times 100\%$$
.

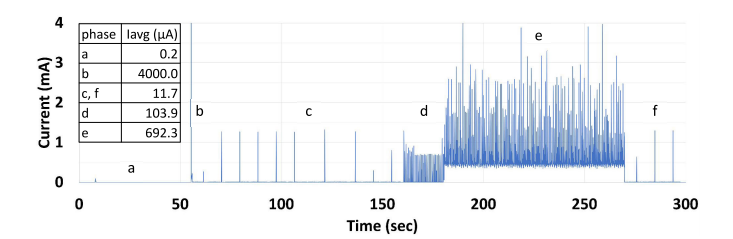


Fig. 6. Transient plot and summary table of the current drawn by the implant from a 3.0-V dc supply. The different phases are: (a) supply is enabled from the source meter, but the implant is still switched off; (b) implant is powered on by removing the external magnet; (c) advertising with 2.5-s interval; (d) connected to the receiver with all the sensors disabled; (e) all the sensors are enabled and the BLE radio is transmitting data; and (f) disconnected and advertising again.

We observed that the packet loss showed a steep rise when the separation was greater than 3 m. This clearly indicates an upper limit for the operational region for the external data aggregator around the animal. This may be slightly reduced by the attenuation through the thin layer of skin. For example, a 5-mm pig skin would have an attenuation of about 3 dB [49] and this would reduce the range to 2 m. While this range is smaller than the industry-standard open-air BLE range, this still allows for several monitoring applications for the animals moving around within confined spaces or carrying a wearable (e.g., collar, harness, and saddle) where the external data aggregator can be placed for data to be recorded to the micro-SD card. Based on the use case, the external aggregator can include stronger transceivers and batteries to transmit the data to further distances.

B. Power Consumption

We employed several software improvements as discussed in Section III to reduce the power requirements of various multimodal sensors, the microcontroller, and the radio. We measured the supply current drawn from a 3.0-V dc supply using a source meter (Model 2450, Keithley Instruments, Cleveland, OH, USA). The overall power consumption of the implant with all the sensors active and transmitting data has reduced to 0.7 mA (Fig. 6) which is one-third of the value we previously reported [40] despite the addition of new modalities. The CG-320B battery lasted for approximately 20 h during in vitro tests of continuous sensor reading and data transmission using our custom external receiver. With appropriate duty cycling, the operation duration between recharges can be extended. For example, collecting one minute of data every hour would extend the operation time to 50 days.

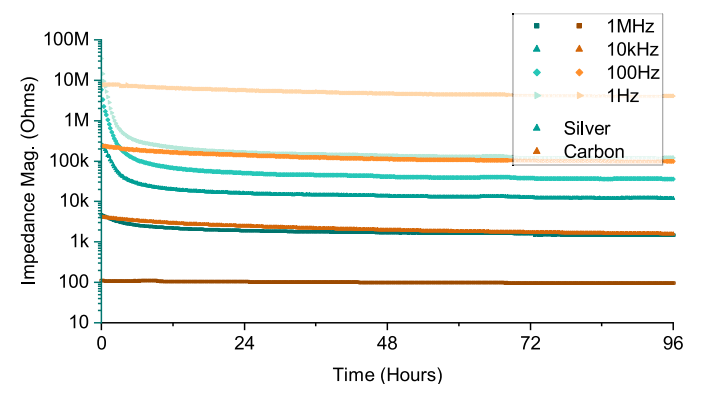


Fig. 7. Impedance magnitude of the implant test samples with silver electrodes and carbon electrodes that were soaked in a saline solution, showing convergence within 24 h.

C. Electrode Characterization

As the interface between the tissue and the ECG AFE, the electrodes' characteristics are important for the system's performance and reliability. In order to test this, we created six test samples using each electrode material (i.e., silverand carbon-based conductive epoxies) and placed them in a 0.9% saline solution. The electrode test samples were identical in shape and form to the ones used for the implant system. Instead of the implant electronics, these were connected to a portable potentiostat system (PalmSens 4, PalmSens BV, Houten, The Netherlands) for electrochemical characterization. The electrodes were left in the saline solution for four days in order to examine any changes that might occur in vivo. As expected (because it has been reported in the literature), significant changes in the impedance magnitude occurred within the first 24 h of being exposed to the wet environment, but the interface stabilized after that (Fig. 7). We used electrochemical impedance spectroscopy (EIS) to characterize the electrodes and observe the changes. EIS involved using low-voltage ac within a range of frequencies (1 Hz–1 MHz, in this case) to measure the impedance between the electrodes at each end of the implant (Fig. 8). This process was repeated five times for each of the six test samples before and after a 24-h soaking period. A Levenberg-Marquardt algorithm (PalmTrace 3.9, PalmSens BV) fit the impedance data to a standard electrode model (Randles circuit shown in Fig. 8) consisting of three elements: the saline resistance (R_s) , the double-layer capacitance $(C_{\rm dl})$, and the charge-transfer resistance (R_{ct}) .

The carbon and silver electrodes demonstrated different characteristics. The average (n=3) combined charge-transfer resistance of the carbon electrodes was $708\pm1170~\mathrm{k}\Omega$ before the soaking and $36.8\pm23.1~\mathrm{k}\Omega$ after. In comparison, the silver electrodes had a higher average (n=3) of $15.8\pm35.2~\mathrm{M}\Omega$ before and $154\pm87.8~\mathrm{k}\Omega$ after. The silver electrodes did have a lower average (n=3) combined double-layer capacitance of $37.7\pm21.1~\mathrm{pF}$ before the 24-h period and $301\pm412~\mathrm{pF}$ afterward, which contrasts with the carbon electrode's average (n=3) double-layer capacitance of 4.57 ± 1.60 and $3.76\pm1.54~\mathrm{nF}$, respectively. While both electrodes are suitable for use with this design, these results indicate that the carbon

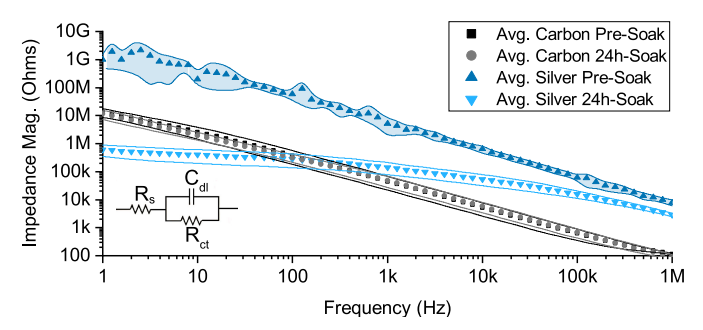


Fig. 8. Average (n=3) electrochemical impedance spectra (with the standard deviation range) of the implant testing samples for the two different electrode materials before and after soaking in a 0.9% saline solution for 24 h with an inset of the equivalent circuit used to fit the spectra.

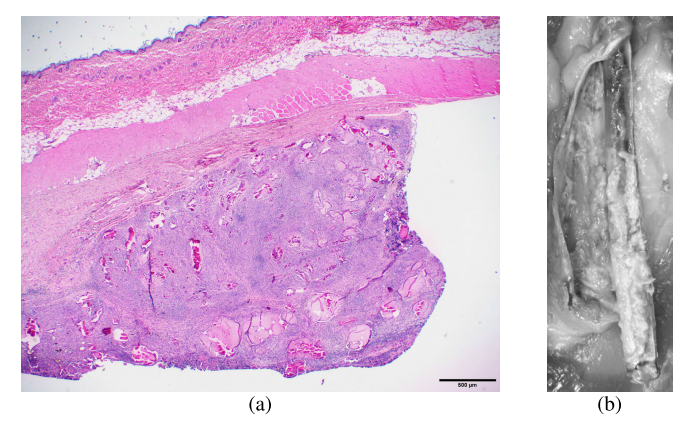


Fig. 9. (a) Histological sample of the fibrous tissue that encapsulated the implant. (b) Implant is being removed from the inner surface of the rat skin and showing an increased formation of fibrous tissue around the portion of the implant containing the battery.

electrodes are more stable than the silver electrodes. Furthermore, the lower resistance of carbon electrodes means that ECG measurements will be affected less by Johnson (thermal) noise and the input impedance of AFE. The silver electrodes may be better suited for BioZ applications, due to their lower capacitance.

D. In Vivo Experiments for Tissue Reaction

Two in vivo experiments were performed to evaluate the integrity of the implant's packaging as well as its behavior in common rats (Rattus norvegicus). One long-term in vivo experiment was run using the implants having silver epoxy electrodes with a histological analysis afterward. Five implants with the silver epoxy electrodes remained in five individual rats (implanted at the age of 11 weeks) for 69 days. All the rats indicated normal overall health. All the implants were surrounded by some fibrous tissue which still provided a successful PPG and ECG measurement. Some of the implants caused localized granulomatous inflammation [closely imaged in Fig. 9(a)]. The fibrous encapsulation was more pronounced around the portion of the implant containing the CR435 battery [Fig. 9(b)]. This probably was due to PMMA at that region being thinner because of the thicker battery volume. This speculation was supported by the presence of systemic lymphoid hyperplasia due to the immune system being provoked by the

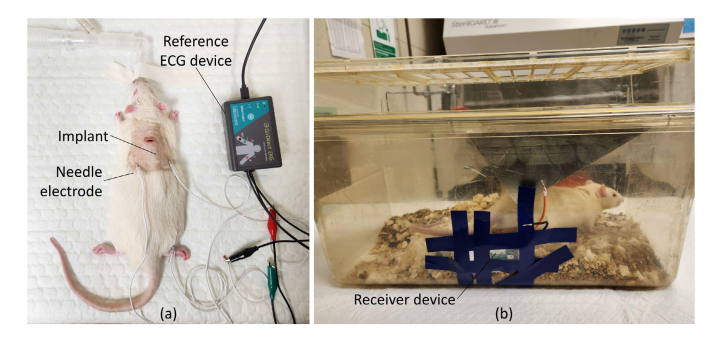


Fig. 10. Experimental setup of: (a) validation experiment on anesthetized rat and (b) data collection from a freely moving rat in a cage.

contents of electrochemical byproducts caused by the interaction between extracellular fluid and battery material [50], [51]. One of the rats did have localized lytic necrosis that was probably the result of a secondary infection due to the rat maintaining an open wound for a longer period. This can happen if the rat manages to reach the implantation site and scratches at it. This finding is supported by the presence of a crusting lesion over the implant site on just that rat. This initial experiment motivated us to coat all internal components, especially the batteries, with a secondary layer of coating (biomedical epoxy).

A second experiment involved the long-term performance of implants that tested the viability of the carbon electrodes and improvements from the previous experiment. The results from six rats (implanted at the age of 12 weeks) after 69 days were better than the first experiment. All the rats had some minor fibrosis around the implant, and there was evidence of the immune system having been stimulated due to the presence of the implant as a foreign material, but crucially there was no swelling or necrosis. The observed fibrosis is actually beneficial because it helps keep the implant in place. Therefore, its occurrence is useful as long as inflammation is not present. Overall, the results were positive and indicated that the implant and its packaging are suitable for long-term implantation.

E. In Vivo Data Collection Experiments

We performed two sets of experiments on 12-week-old Wistar rats (*Rattus norvegicus domestica*): 1) short-duration using anesthetized animals with concurrent gold-standard measurements for data validation and 2) longer duration physiological data collection using awake and untethered animals in a housing cage. The veterinary operating room as well as the postoperative room where the rat cages were housed had a temperature of 23 °C controlled by a central air conditioner.

1) Validation of Implant Data: We collected simultaneous implant data (referred to as CAP ECG/PPG/ACC in Figs. 14–17 and Tables I and II) and gold-standard ECG data (referred to as VER ECG in the presented figures) using a commercial device (Go Direct EKG Sensor, Vernier Software & Technology, Beaverton, OR, USA) from an anesthetized rat [Fig. 10(a)]. During this experiment, the rat was anesthetized using isoflurane, and the site of implantation was shaved for better visual observations. The implant was

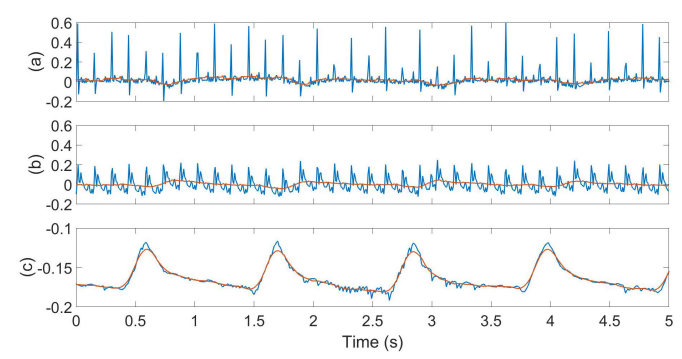


Fig. 11. Extraction of breathing artifacts from raw physiological signals: (a) Vernier ECG; (b) implant ECG; and (c) implant PPG.

inserted subcutaneously on the dorsal side. To record the reference gold-standard ECG signal, three needle electrodes were attached subdermally (two needles inserted adjacent to the implant and the third one in the right leg). Finally, we established the BLE connection between the implant and an external data aggregator to record data for 5 min.

The respiratory rate was easily determined as the mechanical movement of the tissue with the lung expansion modulated all the raw signals, especially the PPG signal (respiratory artifacts causing baseline wander as defined in [52]). We used a 19-point moving average (MAV) filter to extract the respiratory baselines from the ECG signals recorded from both devices with a sampling frequency of 128 Hz (Fig. 11). As the sampling frequency of the PPG signal was 100 Hz, we used a 15-point MAV filter. The length of the filter was chosen to eliminate the heart pulses from the baseline by placing the frequency of the first notch from the MAV filter near the average HR (6.73 Hz in the case of ECG and 6.67 Hz in the case of PPG). We have also analyzed the accelerometer data for breathing motion. Although the accelerometer was sampled only at 10 Hz to conserve power, a five-point MAV filter removed the noise and extracted the BR as an alternative method (see Fig. 12).

Once the baseline drift is subtracted from the raw ECG from the two separate ECG devices (implant and the gold standard), we obtained the clean ECG signals (Fig. 13) which clearly coincided with each other. As the PPG signal was more heavily affected by the breathing artifact, a finite impulse response (FIR) filter with a passband between 6 and 8 Hz was used to obtain the clean heart pulses. Finally, we performed peak detection using a library function findpeaks in MATLAB (Mathworks, Natick, MA) on the filtered ECG/PPG signals and their baselines to get the R-to-R and respiratory intervals, respectively (Figs. 12 and 13).

To compare the extracted HR and BR values in beats per minute (BPM) with the gold standard, the signals are divided into 5- and 15-s windows, respectively. Figs. 14(a) and 15(a) show the transient plots of the average HR and BR from each of these windows along with a bar plot showing the mean and standard deviation (SD) of those values. Figs. 14(b) and (c) and 15(b)–(d) show the Bland–Altman plots that demonstrate the relation between the difference of the test signal from the reference gold-standard signal and the mean of the two signals [53]. As we did not have a gold standard for the BR,

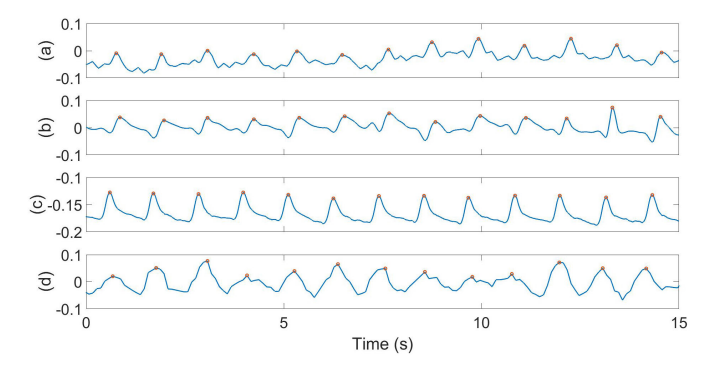


Fig. 12. Extraction of BR from simultaneous signal baselines: (a) Vernier ECG; (b) implant ECG; (c) implant PPG; and (d) implant accelerometer data.

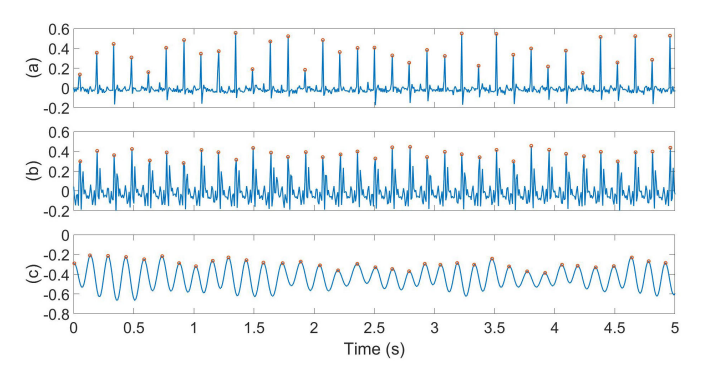


Fig. 13. Extraction of HR from simultaneous filtered signals: (a) Vernier ECG; (b) implant ECG; and (c) implant PPG. The synchrony of the peaks indicates the successful assessment of HR and the potential to calculate the PTT as an exploratory parameter.

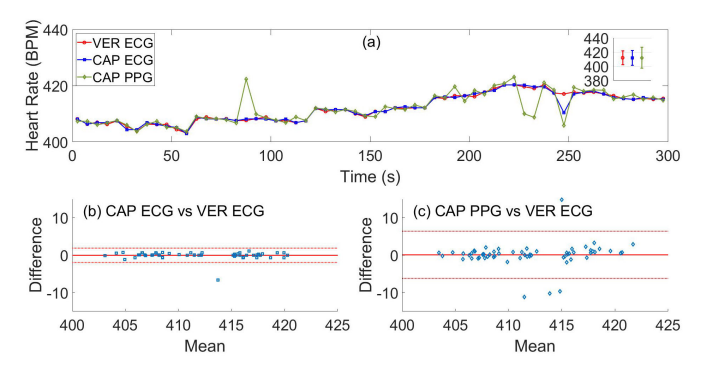


Fig. 14. (a) Transient plot showing the trace of mean HR from each 5-s window of the three signals along with a bar plot showing the mean \pm SD in the inset. The bottom ones show the Bland–Altman plots to compare the HR values from: (b) implant ECG and (c) implant PPG with Vernier ECG.

we used the BR extracted from the implant PPG baseline as a reference in our analysis. The statistical analysis on the extracted values is summarized in Table I, which shows the matching of the mean HR and BR values and that the mean absolute error (MAE) is less than 2 beats per minute (BPM) in all cases.

2) Demonstration of Long-Term Operation: As a proof-of-concept demonstration of the longer-term data collection from a freely moving animal, we inserted a sterile implant subcutaneously in a rat under anesthesia. Then, we let the rat wake up in its usual housing cage and attached the receiver board to the

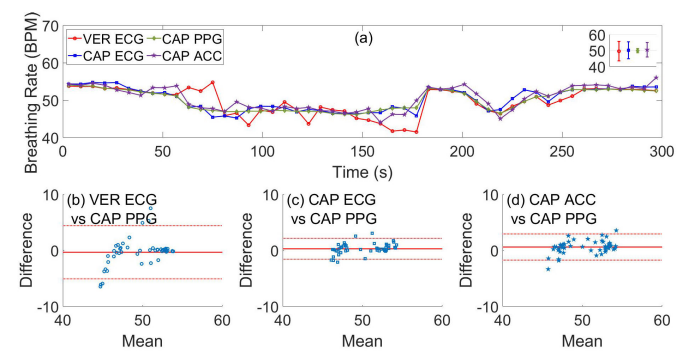


Fig. 15. (a) Transient plot showing the trace of mean BR from each 15-s window (with 67% overlap) of the four signals along with a bar plot showing the mean \pm SD in the inset. The bottom ones show the Bland–Altman plots to compare the BR values from: (b) Vernier ECG; (c) implant ECG; and (d) implant ACC with implant PPG.

TABLE I STATISTICAL RESULTS FROM THE ANESTHETIZED RAT

Parameter	Source signal	Mean	SD	MAE
	VER ECG	411.90	9.80	-
HR (BPM)	CAP ECG	411.84	10.41	0.41
	CAP PPG	411.97	14.57	1.57
BR (BPM)	CAP PPG	49.96	1.32	_
	VER ECG	49.63	6.03	1.39
	CAP ECG	50.24	5.27	0.69
	CAP ACC	50.56	4.48	1.03

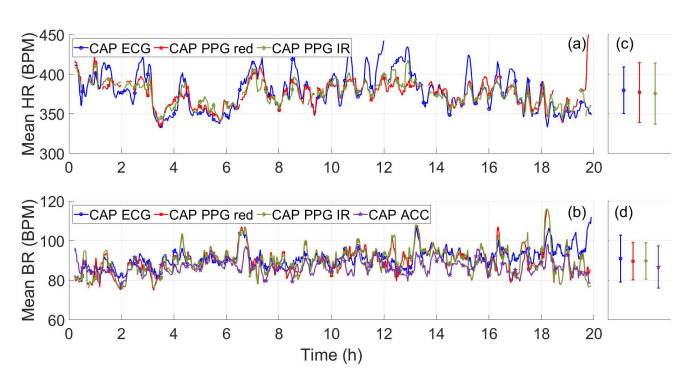


Fig. 16. Transient plots showing the trace of the mean: (a) HR and (b) BR from each 10-min window of the three signals collected from the freely moving rat along with bar plots showing the mean \pm SD of the: (c) HR and (d) BR values.

outer wall of the cage [Fig. 10(b)]. Once the BLE connection was established, we collected ECG, PPG (with red and IR LEDs), accelerometer, and temperature data until the battery in the implant was depleted (after about 20 h).

The HR values were extracted from this data using similar steps as the validation experiment, except that we calculated the signal quality index (SQI) of the HR values in each of the 5-s windows and only use the valid windows based on the algorithm proposed in [54] toward calculating BR (a 15-s window for BR estimation requires three valid 5-s windows in a row). Finally, we averaged the HR and BR values over 10-min periods and presented those in the transients and statistical analysis in Fig. 16 and Table II. Even without any reference measurement, the agreement of the extracted

TABLE II
STATISTICAL RESULTS FROM THE FREELY MOVING RAT

Parameter	Source signal	Mean	SD
HR (BPM)	CAP ECG	379.68	29.52
	CAP PPG red	376.82	37.59
	CAP PPG IR	375.51	38.62
BR (BPM)	CAP ECG	90.91	11.83
	CAP PPG red	89.58	9.40
	CAP PPG IR	89.74	9.21
	CAP ACC	86.70	10.61

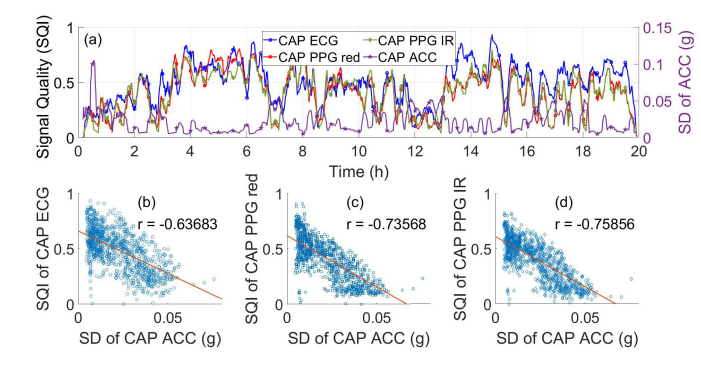


Fig. 17. (a) Transient plots of the SQI of the HR values extracted from the three signals and the SD of the ACC data showing the impact of motion artifacts on the physiological signals. (b)–(d) Bottom plots show the correlation of the SQI values with the SD of ACC.

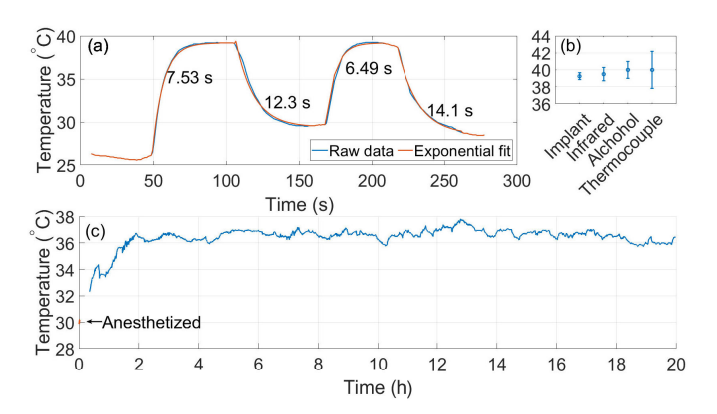


Fig. 18. (a) Transient plot of in vitro temperature showing the time constants of the exponential transitions between ambient and hot water bath. (b) Steady-state readings of various temperature sensors along with their tolerances [40]. (c) Transient plot of subcutaneous temperature from the long-term experiment.

parameters from all the modalities ensures the self-consistent and reliable standalone operation of the implant.

We observed that the PPG signals were more affected by the motion artifacts than the ECG signal, as expected, and thus produced fewer valid windows. We wanted to make sure that this did not originate from any system vulnerability; hence, we compared the average SQI with the SD of the magnitude of acceleration from those 10-min periods and presented that in Fig. 17 which also confirms that ECG is more reliable. Moreover, this result shows promise that the power usage of the implant can be optimized by letting the ECG AFE and IMU run for baseline HR, BR, and IMU-based SQI prediction, and only activating the power-hungry PPG circuit when the SD of ACC data is low enough to generate reliable PTT or SpO₂ data.

We used commercially available and reliable devices for ACC, MAG, and subcutaneous TMP. Since these are not affected by a sensitive interface formed with the tissue, as in the case of ECG and PPG, we only evaluated their successful function by checking their statistical outcomes. Both the measured activity levels under anesthesia and during free movement were within the expected ranges. In addition to the in vivo subcutaneous temperature data, in vitro temperature validation results from [40] are also shown in Fig. 18, which confirms the reliable operation of the sensor. In the in vivo study, we observed a gradual increase in temperature from the anesthetized condition (recorded for a short period following the implantation) to the nominal range (after the rat was placed in the cage), which is expected as the literature suggests [55], [56].

VI. CONCLUSION

This article presents an injectable implant as a multimodal sensing platform targeted at physio-behavioral monitoring in animals. This is the first-ever demonstration of a subcutaneously injectable implant providing simultaneous and wireless measurements of PPG, electroencephalography, TMP, ACC, and MAG. Having multiple sensors has the potential to allow for the extraction of advanced health parameters, the improvement of the signal-to-noise ratio for various signals, and the automation of sensor reconfiguration to prolong the battery life by duty cycling unnecessary sensors. The electronic system encapsulation process is designed to allow refurbishing of the electronics and the battery while keeping biocompatibility as the primary goal. The in vitro experiments demonstrated that the system could transmit data to an external transmitter within three meters of the implant and that the batteries last 20 h with continuous sensor and radio operation. These experiments also showed the superiority of carbon electrodes for biopotential measurements. The in vivo experiments validated the cardiopulmonary health signals in anesthetized and freely moving animal animals. The HR and BR measurements showed an error of less than 2 BPM with respect to the reference values. In addition to its potential in activity tracking, the accelerometer data were proven to provide information about the quality of other signals which is key to dynamic duty cycling. By tracking key physiological and behavioral parameters in animals, such a multimodal injectable implant can be a useful research and management tool for various applications from animal husbandry and veterinary assessments to wellness management and performance monitoring.

REFERENCES

- [1] P. J. O'Brien and J. S. Rand, "Canine stress syndrome," J. Amer. Veterinary Med. Assoc., vol. 186, no. 5, pp. 432–433, Mar. 1985.
- [2] S. I. Johnson, M. Mcmichael, and G. White, "Heatstroke in small animal medicine: A clinical practice review," J. Veterinary Emergency Crit. Care, vol. 16, no. 2, pp. 112–119, May 2006.
- [3] E. Shepard et al., "Identification of animal movement patterns using tri-axial accelerometry," *Endangered Species Res.*, vol. 10, pp. 47–60, Mar. 2008.
- [4] R. Brugarolas et al., "Wearable heart rate sensor systems for wireless canine health monitoring," *IEEE Sensors J.*, vol. 16, no. 10, pp. 3454–3464, May 2016.

- [5] H. J. Williams et al., "Identification of animal movement patterns using tri-axial magnetometry," *Movement Ecology*, vol. 5, no. 1, p. 6, Mar. 2017.
- [6] S. Akter et al., "Impacts of air velocity treatments under summer condition: Part I—Heavy broiler's surface temperature response," *Animals*, vol. 12, no. 3, p. 328, Jan. 2022.
- [7] B. R. Bracio, W. Horn, and D. P. Moller, "Sensor fusion in biomedical systems," in *Proc. 19th Annu. Int. Conf. IEEE Eng. Med. Biol. Soc.* (EMBC), vol. 3, Oct. 1997, pp. 1387–1390.
- [8] D. Morton and P. Griffiths, "Guidelines on the recognition of pain, distress and discomfort in experimental animals and an hypothesis for assessment," *Veterinary Rec.*, vol. 116, no. 16, pp. 431–436, Apr. 1985.
- [9] A. C. Murillo, A. Abdoli, R. A. Blatchford, E. J. Keogh, and A. C. Gerry, "Parasitic mites alter chicken behaviour and negatively impact animal welfare," *Sci. Rep.*, vol. 10, no. 1, p. 8236, May 2020.
- [10] P. Ahmmed, J. Reynolds, A. Bozkurt, and P. Regmi, "Continuous heart rate variability monitoring of freely moving chicken through a wearable electrocardiography recording system," *Poultry Sci.*, vol. 102, no. 2, Feb. 2023, Art. no. 102375.
- [11] L. J. Frewer, A. Kole, S. M. A. V. D. Kroon, and C. D. Lauwere, "Consumer attitudes towards the development of animal-friendly husbandry systems," *J. Agricult. Environ. Ethics*, vol. 18, no. 4, pp. 345–367, Aug. 2005.
- [12] A. Cornish, D. Raubenheimer, and P. McGreevy, "What we know about the Public's level of concern for farm animal welfare in food production in developed countries," *Animals*, vol. 6, no. 11, p. 74, Nov. 2016.
- [13] D. Berckmans, "Precision livestock farming technologies for welfare management in intensive livestock systems," *Revue Scientifique Techn.*, vol. 33, no. 1, pp. 189–196, Apr. 2014.
- [14] N. Ben Sassi, X. Averós, and I. Estevez, "Technology and poultry welfare," *Animals*, vol. 6, no. 10, p. 62, Oct. 2016.
- [15] S. Neethirajan, "Recent advances in wearable sensors for animal health management," Sens. Bio-Sensing Res., vol. 12, pp. 15–29, Feb. 2017.
- [16] M. Foster et al., "Preliminary evaluation of a wearable sensor system for heart rate assessment in guide dog puppies," *IEEE Sensors J.*, vol. 20, no. 16, pp. 9449–9459, Aug. 2020.
- [17] S. P. Hill and D. M. Broom, "Measuring zoo animal welfare: Theory and practice," *Zoo Biol.*, vol. 28, no. 6, pp. 531–544, Nov. 2009.
- [18] A. Jukan, X. Masip-Bruin, and N. Amla, "Smart computing and sensing technologies for animal welfare: A systematic review," ACM Comput. Surveys, vol. 50, no. 1, pp. 1–27, Apr. 2017.
- [19] B. Cugmas, E. Štruc, and J. Spigulis, "Photoplethysmography in dogs and cats: A selection of alternative measurement sites for a pet monitor," *Physiological Meas.*, vol. 40, no. 1, Jan. 2019, Art. no. 01NT02.
- [20] A. Kiourti and K. S. Nikita, "A review of in-body biotelemetry devices: Implantables, ingestibles, and injectables," *IEEE Trans. Biomed. Eng.*, vol. 64, no. 7, pp. 1422–1430, Jul. 2017.
- [21] S. Reichelt et al., "Development of an implantable pulse oximeter," *IEEE Trans. Biomed. Eng.*, vol. 55, no. 2, pp. 581–588, Feb. 2008.
- [22] M. Theodor et al., "Implantable pulse oximetry on subcutaneous tissue," in *Proc. 36th Annu. Int. Conf. IEEE Eng. Med. Biol. Soc.*, Aug. 2014, pp. 2089–2092.
- [23] F. Marefat, R. Erfani, K. L. Kilgore, and P. Mohseni, "Minimally invasive muscle-based recording of photoplethysmogram toward chronic implantation," in *Proc. IEEE Biomed. Circuits Syst. Conf. (BioCAS)*, Oct. 2016, pp. 388–391.
- [24] P. Cong, N. Chaimanonart, W. H. Ko, and D. J. Young, "A wireless and batteryless 10-bit implantable blood pressure sensing microsystem with adaptive RF powering for real-time laboratory mice monitoring," *IEEE J. Solid-State Circuits*, vol. 44, no. 12, pp. 3631–3644, Dec. 2009.
- [25] K. Fricke et al., "In-vivo characterization of left-ventricle pressure-volume telemetry system in swine model," *Biomed. Microdevices*, vol. 18, no. 5, p. 75, Aug. 2016.
- [26] Á. Bjarnason et al., "Implantable measurement system for dairy-cattle monitoring with long recording time," Adv. Sci. Technol., vol. 85, pp. 33–38, Sep. 2012.
- [27] T. Volk et al., "RFID technology for continuous monitoring of physiological signals in small animals," *IEEE Trans. Biomed. Eng.*, vol. 62, no. 2, pp. 618–626, Feb. 2015.
- [28] J.-H. Lee and D.-W. Seo, "Development of ECG monitoring system and implantable device with wireless charging," *Micromachines*, vol. 10, no. 1, p. 38, Jan. 2019.
- [29] M. Theodor et al., "Subcutaneous blood pressure monitoring with an implantable optical sensor," *Biomed. Microdevices*, vol. 15, no. 5, pp. 811–820, Oct. 2013.

- [30] A. Harkin, J. M. O'Donnell, and J. P. Kelly, "A study of VitalViewTM for behavioural and physiological monitoring in laboratory rats," *Physiol. Behav.*, vol. 77, no. 1, pp. 65–77, Sep. 2002.
- [31] A. J. Davidson, F. Aujard, B. London, M. Menaker, and G. D. Block, "Thermochron iButtons: An inexpensive method for long-term recording of core body temperature in untethered animals," *J. Biol. Rhythms*, vol. 18, no. 5, pp. 430–432, Oct. 2003.
- [32] M. Theodor et al., "Implantable accelerometer system for the determination of blood pressure using reflected wave transit time," Sens. Actuators A, Phys., vol. 206, pp. 151–158, Feb. 2014.
- [33] N. V. de Camp, A. Heimann, O. Kempski, and J. Bergeler, "Accelerometer-based assessment of intestinal peristalsis: Toward miniaturized low-power solutions for intestinal implants," *IEEE J. Translational Eng. Health Med.*, vol. 6, pp. 1–7, Sep. 2018.
- [34] T. Weydts, L. Brancato, M. A. Soebadi, D. De Ridder, and R. Puers, "A novel method to investigate bladder wall behavior by acceleration and pressure sensing," *Sens. Actuators A, Phys.*, vol. 280, pp. 376–382, Sep. 2018.
- [35] E. Svendsen, M. Fore, L. L. Randeberg, and J. A. Alfredsen, "Design of a novel biosensor implant for farmed Atlantic salmon (Salmo salar)," in *Proc. IEEE Sensors*, Oct. 2021, pp. 1–4.
- [36] J. M. Valero-Sarmiento, S. Bhattacharya, A. Krystal, and A. Bozkurt, "Towards injectable biophotonic sensors for physiological monitoring of animals," in *Proc. IEEE SENSORS*, Nov. 2014, pp. 503–506.
- [37] J. M. Valero-Sarmiento, J. Reynolds, A. Krystal, and A. Bozkurt, "In vitro evaluation of an injectable EEG/ECG sensor for wireless monitoring of hibernation in endangered animal species," *IEEE Sensors J.*, vol. 18, no. 2, pp. 798–808, Jan. 2018.
- [38] J. M. Valero-Sarmiento, P. Ahmmed, and A. Bozkurt, "In vivo evaluation of a subcutaneously injectable implant with a low-power photoplethysmography ASIC for animal monitoring," *Sensors*, vol. 20, no. 24, p. 7335, Dec. 2020.
- [39] J. Reynolds, P. Ahmmed, and A. Bozkurt, "Preliminary evaluation of an injectable sensor for subcutaneous photoplethysmography in animals," in Proc. IEEE Biomed. Circuits Syst. Conf. (BioCAS), Oct. 2018, pp. 1–4.
- [40] J. Reynolds, P. Ahmmed, and A. Bozkurt, "An injectable system for subcutaneous photoplethysmography, accelerometry, and thermometry in animals," *IEEE Trans. Biomed. Circuits Syst.*, vol. 13, no. 5, pp. 825–834, Oct. 2019.
- [41] D. Huang and Z. Du, "Eight-band antenna with a small ground clearance for LTE metal-frame mobile phone applications," *IEEE Antennas Wireless Propag. Lett.*, vol. 17, no. 1, pp. 34–37, Jan. 2018.
- [42] J. Pan and W. J. Tompkins, "A real-time QRS detection algorithm," *IEEE Trans. Biomed. Eng.*, vol. BME-32, no. 3, pp. 230–236, Mar. 1985.
- [43] G. E. Loeb, R. A. Peck, W. H. Moore, and K. Hood, "BIONTM system for distributed neural prosthetic interfaces," *Med. Eng. Phys.*, vol. 23, no. 1, pp. 9–18, Jan. 2001.
- [44] J. Riistama et al., "Wireless and inductively powered implant for measuring electrocardiogram," *Med. Biol. Eng. Comput.*, vol. 45, no. 12, pp. 1163–1174, Nov. 2007.
- [45] L. Zhou, R. Chmait, Y. Bar-Cohen, R. A. Peck, and G. E. Loeb, "Percutaneously injectable fetal pacemaker: Electrodes, mechanical design and implantation," in *Proc. Annu. Int. Conf. IEEE Eng. Med. Biol. Soc.*, Aug. 2012, pp. 6600–6603.
- [46] T. Hirao and S. Hamada, "Novel multi-material 3-dimensional low-temperature co-fired ceramic base," *IEEE Access*, vol. 7, pp. 12959–12963, 2019.
- [47] P. Ahmmed, J. Reynolds, S. Hamada, P. Regmi, and A. Bozkurt, "Novel 3D-printed electrodes for implantable biopotential monitoring," in *Proc.* 43rd Annu. Int. Conf. IEEE Eng. Med. Biol. Soc. (EMBC), 2021, pp. 7120–7123.
- [48] J. Reynolds, J. M. Valero-Sarmiento, J. Dieffenderfer, and A. Bozkurt, "The viability of conductive medical epoxy as an implantable electrode material," in *Proc. IEEE SENSORS*, Oct. 2017, pp. 1–3.
- [49] B. Zhen, H.-B. Li, and R. Kohno, "Networking issues in medical implant communications," *Int. J. Multimedia Ubiquitous Eng.*, vol. 4, no. 1, pp. 23–38, 2009.
- [50] P. DiEgidio, H. I. Friedman, R. G. Gourdie, A. E. Riley, M. J. Yost, and R. L. Goodwin, "Biomedical implant capsule formation: Lessons learned and the road ahead," *Ann. Plastic Surgery*, vol. 73, no. 4, pp. 451–460, Oct. 2014.
- [51] R. Klopfleisch and F. Jung, "The pathology of the foreign body reaction against biomaterials," J. Biomed. Mater. Res. A, vol. 105, no. 3, pp. 927–940, Mar. 2017.

- [52] P. H. Charlton et al., "Breathing rate estimation from the electrocardiogram and photoplethysmogram: A review," *IEEE Rev. Biomed. Eng.*, vol. 11, pp. 2–20, 2018.
- [53] D. G. Altman and J. M. Bland, "Measurement in medicine: The analysis of method comparison studies," *J. Roy. Statist. Soc. D*, vol. 32, no. 3, pp. 307–317, Sep. 1983.
- [54] C. Orphanidou, T. Bonnici, P. Charlton, D. Clifton, D. Vallance, and L. Tarassenko, "Signal-quality indices for the electrocardiogram and photoplethysmogram: Derivation and applications to wireless monitoring," *IEEE J. Biomed. Health Informat.*, vol. 19, no. 3, pp. 832–838, May 2015.
- [55] A. C. Caro, F. C. Hankenson, and J. O. Marx, "Comparison of thermoregulatory devices used during anesthesia of C57BL/6 mice and correlations between body temperature and physiologic parameters," J. Amer. Assoc. Lab. Animal Sci., vol. 52, no. 5, pp. 577–583, Sep. 2013.
- [56] M. Rufiange, V. S. Y. Leung, K. Simpson, and D. S. J. Pang, "Prewarming before general anesthesia with isoflurane delays the onset of hypothermia in rats," *PLoS ONE*, vol. 15, no. 3, Mar. 2020, Art. no. e0219722.



Parvez Ahmmed (Member, IEEE) received the B.S. degree in electrical and electronic engineering from the Bangladesh University of Engineering and Technology, Dhaka, Bangladesh, in 2014, and the M.S. and Ph.D. degrees in electrical engineering from North Carolina State (NC State) University, Raleigh, NC, USA, in 2019 and 2021, respectively.

He is currently working as a Postdoctoral Research Scholar with the Integrated Bionic MicroSystems (iBionicS) Laboratory, Depart-

ment of Electrical and Computer Engineering, NC State University. His research interests include the design of analog/mixed-signal circuits and integration of physiological sensors into low-power wearable and implantable systems for biomedical health monitoring applications.



James Reynolds (Member, IEEE) received the B.S. degree in engineering from Bob Jones University, Greenville, SC, USA, in 2015, and the M.S. and Ph.D. degrees in electrical engineering from North Carolina State (NC State) University, Raleigh, NC, USA, in 2017 and 2021, respectively.

He is currently researching various topics as a Research Professor with the National Science Foundation Nanosystems Engineering Research Center for Advanced Self-Powered

Systems of Integrated Sensors and Technologies (ASSIST), NC State University. His areas of research, in addition to digital circuit design, include systems integration for biological applications and electrical techniques for studying plant behavior and physiology.



Alper Bozkurt (Senior Member, IEEE) received the master's degree in biomedical engineering from Drexel University, Philadelphia, PA, USA, in 2004, and the Ph.D. degree in electrical and computer engineering from Cornell University, Ithaca, NY, USA, in 2010.

He is a Distinguished Professor with the Department of Electrical and Computer Engineering, North Carolina State (NC State) University, Raleigh, NC, USA, where he is the Founder and the Director of the Integrated Bionic

MicroSystems Laboratory. He is also the Co-Director of the National Science Foundation (NSF) Nanosystems Engineering Research Center for Advanced Self-Powered Systems of Integrated Sensors and Technologies (ASSIST), and the Institute of Connected Sensor Systems (IConS), NC State University.

Dr. Bozkurt received the Calhoun Fellowship from Drexel University, the Donald Kerr Award from Cornell University, the Chancellor's Innovation Award, William F. Lane Outstanding Teacher Award from NC State University, the Best Paper Award from The U.S. Government Microcircuit Applications and Critical Technology Conference and IEEE Body Sensor Networks Conference, the NSF CAREER Award, and IBM Faculty Award, and was included to the Popular Science Magazine 2015 Brilliant 10 List.